Pseudocapacitance of Amorphous TiO 2 Thin Films Anchored to Graphene and Carbon Nanotubes Using Atomic Layer Deposition

7 AUTHORS, INCLUDING:

Xiang Sun
Michigan Technological University
39 PUBLICATIONS   552 CITATIONS

SEE PROFILE

Ming Xie
Wuhan ATMK Super EnerG Technologies
35 PUBLICATIONS   274 CITATIONS

SEE PROFILE

Jonathan Jackson Travis
University of Colorado Boulder
17 PUBLICATIONS   173 CITATIONS

SEE PROFILE

Hongtao Sun
University of California, Los Angeles
36 PUBLICATIONS   775 CITATIONS

SEE PROFILE

Pseudocapacitance of Amorphous TiO₂ Thin Films Anchored to Graphene and Carbon Nanotubes Using Atomic Layer Deposition

Xiang Sun,[†] Ming Xie,[‡] Jonathan J. Travis,[‡] Gongkai Wang,[†] Hongtao Sun,[†] Jie Lian,*[,†] and Steven M. George*[,‡]

[†]Department of Mechanical, Aerospace & Nuclear Engineering, Rensselaer Polytechnic Institute, 110 Eighth Street, Troy, New York 12180, United States

[‡]Department of Chemistry and Biochemistry and Department of Mechanical Engineering, University of Colorado, Boulder, Colorado 80309, United States

ABSTRACT: Amorphous TiO₂ thin films were conformally coated onto the surface of both graphene (G) and multiwalled carbon nanotube (CNT) samples using atomic layer deposition (ALD). An ultrathin Al₂O₃ adhesion layer was employed to obtain the conformal TiO₂ ALD films. Using 1 M KOH as the electrolyte, the electrochemical characteristics of TiO₂ ALD films grown using 25 and 50 TiO₂ ALD cycles were then determined using cyclic voltammetry, galvanostatic charge/discharge curves, and electrochemical impedance spectroscopy. Because the TiO₂ ALD films were ultrathin, the poor electrical conductivity and low ionic diffusivity of TiO₂ did not limit the ability of the TiO₂ ALD films to display high specific capacitance. The specific capacitances of the TiO₂ ALD-coated G and CNT samples after 50 TiO₂ ALD cycles were 97.5 and 135 F/g, respectively, at 1 A/g. The pseudocapacitance of the TiO₂ ALD films greatly exceeded the electric double layer capacitance of the uncoated G and CNT samples. The galvanostatic charge/discharge experiments also revealed that the charge storage was dependent on the thickness of the TiO₂ ALD film. This observation argues that the pseudocapacitance is derived largely from the TiO₂ bulk and is not limited to the TiO₂ surface. The molar ratio of stored charge to TiO₂ was estimated to be in the range of 0.03−0.08 (mol stored charge/mol TiO₂) for the various TiO₂ ALD-coated G and CNT samples. An optimized asymmetric cell was also developed based on TiO₂ ALD-coated CNT as the positive electrode and uncoated CNT as the negative electrode. This energy storage device could be reversibly operated over a wide voltage range of 0−1.5 V in the aqueous 1 M KOH electrolyte. An energy density of 4.47 W·h/kg was achieved on the basis of the total weight of both electrodes. This energy density was ∼4 times higher than the symmetric CNT cell. The TiO₂ ALD-coated G and CNT electrodes and the asymmetric cell based on the TiO₂ ALD-coated electrode exhibited excellent stability over >1000 cycles. The results of this study demonstrate that metal oxide ALD on high surface area conducting carbon substrates can be used to fabricate high energy storage supercapacitors.
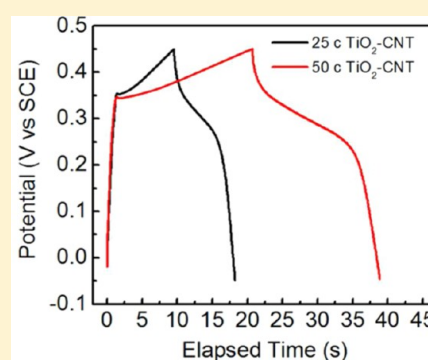
I. INTRODUCTION

Recent advances in nanotechnology allow for the fabrication of new metal oxide nanomaterials for energy-related applications. Nanothin metal oxides for electrochemical energy storage have much shorter diffusion distances required for ion storage and can overcome low diffusion coefficients. The slow insertion/extraction of ions in bulk metal oxide materials significantly restricts the electrochemical kinetics. For example, the diffusion coefficient for Li ions in the TiO₂ crystal lattice is only 10^{-13}–10^{-17} cm²/s.[1] Although this slow transport would be a problem in bulk TiO₂, excellent performance of TiO₂ as an anode in Li ion battery was recently observed with small TiO₂ nanoparticles on graphene (G) substrates.[2] Ultrathin TiO₂ nanosheets[3] and nanoporous amorphous TiO₂ films[4] have also displayed fast Li insertion/extraction processes. In addition, large pseudocapacitance in TiO₂ was demonstrated for TiO₂ nanoparticles on G substrates.[5] High pseudocapacitance in TiO₂ was also observed in porous TiO₂ films[6] and when the TiO₂ particle sizes were below 10 nm.[1]

The low electrical conductivity of metal oxides also restricts electrochemical performance. For example, fully oxidized single crystal rutile TiO₂ is an insulator with a resistivity on the order of 1×10^{13} Ω cm at room temperature.[7] To circumvent this high resistivity, ultrathin films of metal oxides can be deposited on highly conductive electrode supports, such as conductive carbon. The nanothin metal oxide material allows electrons to be transported from the conductive carbon to the metal oxide. Ultrathin TiO₂ coatings on multiwalled CNTs have been shown to exhibit excellent electrical conductance.[8] The electrical conductance of TiO₂ in TiO₂/CNT nanocrystalline composites also allows the TiO₂ to display substantial pseudocapacitance.[9]

Another important factor for electrochemical energy storage by Li ion batteries or pseudocapacitors is the surface area of the

electrode substrate. For example, the large surface area of ~400 m²/g for CNTs and G allows them to serve as ideal substrates for the deposition of metal oxide materials. Their excellent electrical conductivity of ~1000 S/cm and open architecture also lead to efficient electron and ion transport behavior. Several recent reviews have highlighted the enhanced electrochemical performance in carbon/metal oxide composite electrodes.[10−13]

Atomic layer deposition (ALD) is an important thin film growth technique that utilizes sequential self-limiting surface reactions to deposit ultrathin films with Ångstrom-level control.[14] ALD is also able to deposit conformal thin films on very high-aspect-ratio substrates[15,16] or nanoparticles.[17,18] In addition, the chemical reactions in ALD form strong covalent linkages between the ALD film and the underlying substrate. These covalent linkages can significantly enhance the stability of the deposited metal oxide ALD films. ALD can more precisely control the size, morphology, and crystallinity of films or nanoparticles than wet chemical methods such as sol−gel, hydrothermal, and electroplating processing.[19−21]

We have demonstrated TiO_2 ALD on G and CNTs for electrochemical energy storage using Li ion batteries or pseudocapacitance supercapacitors. We have recently shown that TiO_2 ALD on G can serve as an excellent anode for Li ion batteries and leads to improved charge/discharge cycling performance.[2] We have also demonstrated the controllable ALD of TiO_2 nanoparticles on G sheets.[5] The TiO_2 ALD-G nanocomposites exhibited high specific capacitances even at fast charge/discharge rates.[5]

In the current work, we prepare continuous TiO_2 ALD films on the surfaces of G and CNT using an Al_2O_3 adhesion layer. Compared with TiO_2 nanoparticles, a thin continuous TiO_2 ALD film can more completely cover the high surface area of G and CNT substrates. The control of the TiO_2 film thickness by ALD can also maintain the minimum desired thickness for optimal charge and electron transport. We then measure the capacitance properties of the TiO_2 ALD-coated G and CNT electrodes. Because of the pseudocapacitance of TiO_2, the specific capacitances of the TiO_2 ALD-coated G and CNT electrodes are shown to be much higher than the uncoated G and CNT electrodes. In addition, an asymmetric supercapacitor is fabricated by pairing a TiO_2 ALD-coated CNT electrode with a CNT electrode. This asymmetric cell exhibits a much higher energy density than the energy density of the symmetric cell based on CNT electrodes.
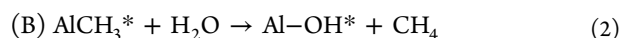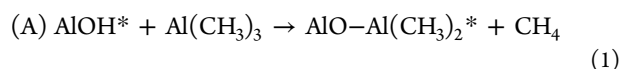
II. EXPERIMENTAL SECTION

A. ALD of Amorphous TiO_2 Films on G and CNT Samples. TiO_2 ALD films were grown on G or CNT powders using a rotary ALD reactor.[22,23] The rotary reactor agitates the powders during ALD and prevents particle aggregation. G sheets were produced by thermal exfoliation of as-synthesized graphite oxide (GO) powders prepared by the Hummers method.[24−26] Multiwalled CNTs were purchased from Sigma-Aldrich.

TiO_2 ALD on G and CNTs has nucleation difficulties because the basal planes of G and the sp^2 surfaces of CNTs are unreactive.[23] A distribution of TiO_2 nanoparticles is produced when the TiO_2 ALD nucleates and grows only at defect sites on the G surface.[5] However, a thin layer of Al_2O_3 can serve as an adhesion layer. The Al_2O_3 adhesion layer was prepared by using sequential exposures of NO_2 and trimethylaluminum (TMA).[23,27] The nitrogen in NO_2 behaves as a Lewis base

and attaches to the graphene surface via electron lone pair interactions that leave oxygen atoms accessible for reaction to TMA. Several cycles of NO_2 and TMA can produce a thin Al_2O_3 adhesion layer.
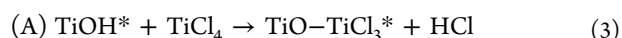
For the NO_2/TMA nucleation treatment, commercial purity grade NO_2 (99.5%) was acquired from Airgas, and TMA (97%) was obtained from Sigma-Aldrich. To form the Al_2O_3 adhesion layer, 10 cycles of NO_2/TMA were performed at 180 °C. The NO_2/TMA functionalization was performed with the following sequence: (i) exposure to NO_2 to set pressure of 1 Torr for 120 s; (ii) evacuation of excess NO_2; (iii) exposure to TMA to set pressure of 1 Torr for 120 s; and (iv) evacuation of excess TMA. This sequence defines one cycle of the NO_2/TMA nucleation procedure.

After NO_2 treatment, Al_2O_3 ALD was performed utilizing trimethylaluminium (TMA) and H_2O as the precursors:[28−31]

$$\text{(A)} \quad AlOH^* + Al(CH_3)_3 \rightarrow AlO{-}Al(CH_3)_2^* + CH_4 \tag{1}$$

$$\text{(B)} \quad AlCH_3^* + H_2O \rightarrow Al{-}OH^* + CH_4 \tag{2}$$

where the asterisk indicates the surface species. The performance of the A and B reactions constitutes one Al_2O_3 ALD cycle. HPLC (high performance liquid chromatography) grade H_2O was obtained from Sigma-Aldrich. The Al_2O_3 ALD reaction sequence was (i) dose TMA to 1.0 Torr for 120 s; (ii) evacuate reaction products and excess TMA; (iii) dose N_2 to 20.0 Torr for 60 s and then evacuate N_2 (repeat 5 times); (iv) dose H_2O to 1.0 Torr for 120 s; (v) evacuate reaction products and excess H_2O; and (vi) dose N_2 to 20.0 Torr for 60 s and then evacuate N_2 (repeat 5 times). This sequence constitutes one AB cycle of Al_2O_3 ALD. The Al_2O_3 ALD was performed for 5 cycles at 180 °C.

TiO_2 ALD was then performed on the Al_2O_3 adhesion layer using utilizing titanium tetrachloride ($TiCl_4$) and H_2O as precursors:[32]

$$\text{(A)} \quad TiOH^* + TiCl_4 \rightarrow TiO{-}TiCl_3^* + HCl \tag{3}$$

$$\text{(B)} \quad TiCl^* + H_2O \rightarrow Ti{-}OH^* + HCl \tag{4}$$

The performance of the A and B reactions constitutes one TiO_2 ALD cycle. $TiCl_4$ (99.8%) was obtained from Strem Chemicals. The TiO_2 ALD reaction sequence was (i) dose $TiCl_4$ to 1.0 Torr for 120 s; (ii) evacuate the reaction products and excess $TiCl_4$; (iii) dose N_2 to 20.0 Torr for 60 s and then evacuate N_2 (repeat 5 times); (iv) dose H_2O to 1.0 Torr for 120 s; (v) evacuate the reaction products and excess H_2O; and (vi) dose N_2 to 20.0 Torr for 60 s and then evacuate N_2 (repeat 5 times). The TiO_2 ALD was performed at 120 °C.

B. Structural and Electrochemical Characterization. The surface, morphological, structural, and microstructural properties of the TiO_2 ALD-coated G and CNT nanocomposites were determined using a variety of materials characterization techniques. These techniques included X-ray diffraction (XRD), thermogravimetric analysis (TGA), BET surface area measurement, X-ray photoelectron spectroscopy (XPS), scanning electron microscopy (SEM), and transmission electron microscopy (TEM). XRD measurements were performed using a PANanalytical X-ray diffraction system. TGA measurements were performed in air at atmospheric pressure from 30 to 700 °C at a heating rate of 10 °C/min in a TA Instruments TGA-Q50.

The surface area and pore size distribution were measured using a Quantachrome AUTOSORB-1 instrument. The samples were heated at 200 °C under vacuum for 12 h before testing. TEM images were obtained using a JEOL JEM-2010 instrument with an operating voltage of 200 kV. A Carl Zeiss Ultra 1540 dual beam FIB/SEM system was used to examine the morphology of the samples. The XPS measurements were recorded on a PHI 5000 Versa Probe system.

A three-electrode testing protocol was employed to evaluate the electrochemical performance of the TiO_2 ALD-coated G and CNT nanocomposites as electrode materials for supercapacitor applications. The three-electrode testing cell was constructed using a working electrode, a platinum wire as a counter electrode, and a saturated calomel electrode (SCE) reference electrode. A 1 M KOH solution was employed as the aqueous electrolyte. A 1 M $NaSO_4$ solution was also attempted as the aqueous electrolyte but did not yield significant specific capacitance. The working electrode was prepared by mixing the active materials, carbon black, and PTFE at a weight ratio of 80:10:10 with a small amount of ethanol.

After sonication for 1 h, the working electrode slurry was pasted onto circular nickel foam (Novamet Specialty Products Corp.). This sample was then dried at 120 °C overnight and compressed by a hydraulic presser. For the assembly of the asymmetric cell, the mass ratios of TiO_2/CNT to CNT were 0.75 and 0.66 for 25 and 50 TiO_2 ALD cycles, respectively. The optimum mass ratios were determined from the specific capacitances of the TiO_2/CNT and CNT samples. The electrodes were separated by a porous polypropylene separator (Celgard 3501) and sealed in a coin cell. The electrochemical testing was performed using a potentiostat VersaSTAT 4 from Princeton Applied Research.

III. RESULTS AND DISCUSSION

A. Physical Characterization of TiO_2 Films on G and CNT Samples. Figure 1a shows the XRD patterns from the TiO_2 ALD on the Al_2O_3 adhesion layer on the G powder. Only a weak and broad peak at ~24° is observed after 25 and 50 TiO_2 ALD cycles. This peak is assigned to the disordered graphene layer stacking as observed in both thermal exfoliated[33,34] and chemical reduced[35] graphene sheets. Figure 1b shows the XRD patterns from the TiO_2 ALD on the Al_2O_3 adhesion layer on the CNT sample. The original and TiO_2 ALD-coated CNT samples exhibited a strong peak at ~26°. This peak is assigned to the well-ordered graphitic structure of the CNT.[36] No peaks could be observed in Figure 1a or 1b for the crystalline anatase or rutile phases of TiO_2. The absence of these peaks is consistent with amorphous TiO_2 on the Al_2O_3 adhesion layer on the G powders and CNT samples.

In our earlier work on TiO_2 on G without the Al_2O_3 adhesion layer, the TiO_2 nucleated at distinct locations and grew as TiO_2 nanoparticles.[5] XRD studies revealed that these nanoparticles were crystalline with the anatase structure.[5] Consequently, the Al_2O_3 adhesion layer has produced a continuous TiO_2 coating and also yielded the amorphous structure. Usually TiO_2 ALD forms an amorphous film at 100–140 °C. The anatase phase can be formed at deposition temperature above 160 °C.[37] The Al_2O_3 adhesion layer has helped to produce an amorphous TiO_2 film that may exhibit superior charge storage capability than the crystalline TiO_2 film.[38–42]

The presence of TiO_2 on the G and CNT samples was confirmed by XPS. Figure 2a shows the XPS survey scan of the
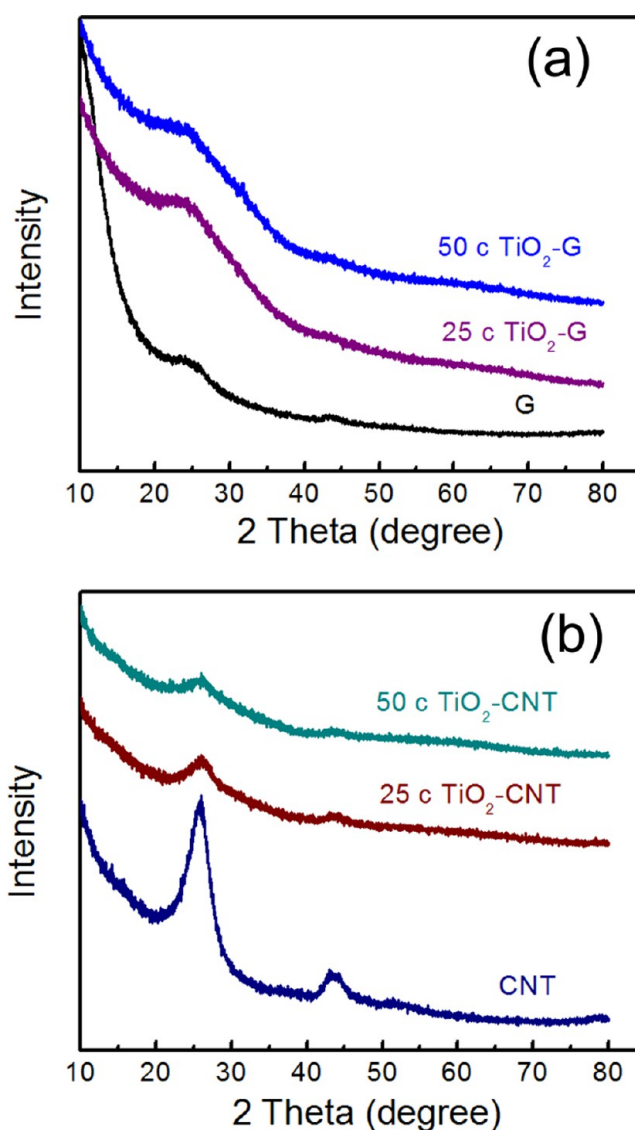

Figure 1. XRD scans of (a) G and TiO_2 ALD on Al_2O_3 adhesion layer on G and (b) CNT and TiO_2 ALD on Al_2O_3 adhesion layer on CNT.

TiO_2 ALD on the Al_2O_3 adhesion layer on the CNT samples. XPS signals are observed for carbon, oxygen, titanium, aluminum, and chlorine with at. % of 41.3, 37.9, 12.8, 4.0, and 2.2, respectively. The chlorine is attributed to incomplete surface reactions during the TiO_2 ALD growth process. The aluminum peak is assigned to the Al_2O_3 adhesion layer. Figure 2b shows the XPS spectra of the Ti 2p peaks located at 464.9 and 459.2 eV. The peak separation of 5.7 eV is in excellent agreement with the reported values for TiO_2.[43–45] The O:Ti at. % ratio is higher than expected from the TiO_2 stoichiometry. This higher ratio is attributed to additional O XPS signal resulting from the underlying Al_2O_3 adhesion layer.

Figure 3 shows the TGA results that were used to obtain the TiO_2 mass loading on the G and CNT samples. A continuous weight loss is observed for samples at temperature above 100 °C. This weight loss is attributed to release of H_2O and chemisorbed hydroxides as the temperature increases.[46] Large weight losses were then observed at the oxidation temperatures of ~450 °C for the G sample and ~550 °C for the CNT sample. The higher thermal stability for the CNT samples
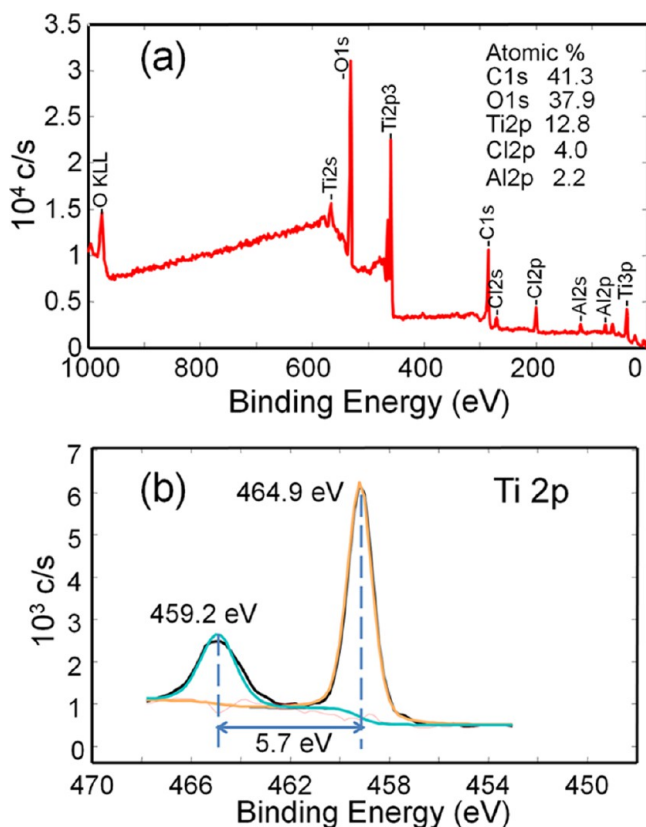
Figure 2. XPS spectra after 50 TiO_2 ALD cycles on the Al_2O_3 adhesion layer on the CNT samples: (a) XPS survey spectrum and (b) Ti 2p region of XPS spectrum.
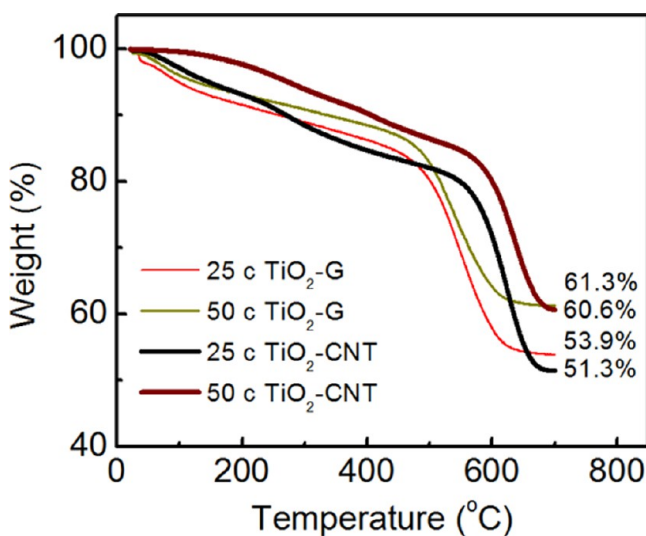

Figure 3. TGA results for TiO_2 ALD on the Al_2O_3 adhesion layer on G and CNT.

results from its more graphitic structure with fewer surface defects in good agreement with previous reports.[47]

The weight percentage of the Al_2O_3 adhesion layer was obtained from the weight difference of the samples before and after the Al_2O_3 ALD coating. The mass of the original G and CNT samples placed in the rotary ALD reactor was ∼100 mg. The mass gain for both the G and CNT samples after the deposition of the Al_2O_3 adhesion layer was ∼10%. The mass gain was similar for the G and CNT samples because the

surface areas of both samples were very comparable in the range of 400−450 m^2/g.

The mass percentage of the TiO_2 ALD together with the Al_2O_3 adhesion layer was determined from the weight after annealing to 700 °C in the TGA experiments. Based on the mass of the Al_2O_3 adhesion layer from the weight difference and the combined TiO_2 ALD and Al_2O_3 ALD weight % from the TGA measurements, the mass loading of TiO_2 was calculated to be 49.3 and 57.43 wt % for the 25 and 50 TiO_2 ALD cycle TiO_2-G samples, respectively. The mass loading of TiO_2 was also calculated to be 46.4 and 56.66 wt % for the 25 and 50 TiO_2 ALD cycle TiO_2−CNT samples, respectively. These calculations assume that the carbon is completely removed following annealing to 700 °C. This assumption is reasonable because there was negligible change in sample weights at temperatures above 700 °C in additional TGA experiments.

Uniform amorphous TiO_2 ALD films were coated onto the G and CNT surfaces. An SEM micrograph of G coated with an Al_2O_3 adhesion layer and 50 cycles of TiO_2 ALD is shown in Figure 4. The graphene powder is uniformly covered with a
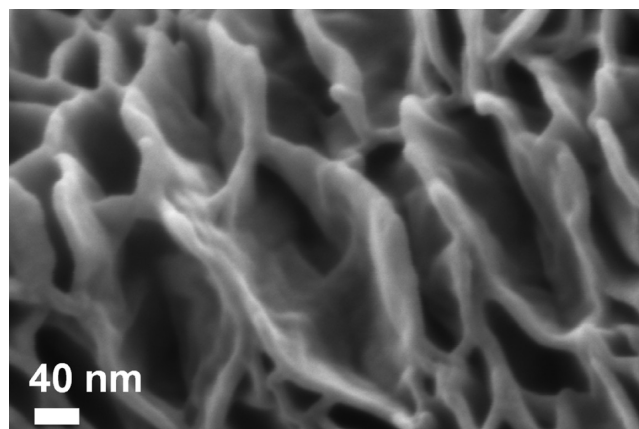

Figure 4. SEM micrographs of G after 50 cycles of TiO_2 ALD on the adhesion layer on G.

smooth TiO_2 ALD film. In contrast to the observations for TiO_2 ALD on G without an Al_2O_3 adhesion layer,[5] no nanoparticles are present. Compared with the original graphene layer, the graphene wrinkles are ∼12−16 nm in thickness after the ALD. This thickness results from a thickness of ∼6−8 nm for the TiO_2 ALD and Al_2O_3 adhesion layer on each side of the graphene wrinkles.

Figure 5 shows the wall of the CNT coated with an Al_2O_3 adhesion layer and 50 cycles of TiO_2 ALD. A very uniform and conformal composite film is observed with a total thickness of ∼13 nm. There are no gaps or voids in the films or at the interfaces. This thin composite film should not affect the electron transport. Electron conduction through these films should be high resulting from electron tunneling.[48]

The thickness of the ALD layer on the CNT coated with an Al_2O_3 adhesion layer and 50 cycles of TiO_2 ALD is larger than the thickness predicted by the growth rates for Al_2O_3 ALD and TiO_2 ALD on flat substrates. The growth rate of Al_2O_3 ALD on flat substrates is 1.1−1.2 Å/cycle at 180 °C.[29−31] The growth rate of TiO_2 ALD on flat substrates is 0.4 Å/cycle at 120 °C.[32] However, earlier studies have reported ALD growth rates on high surface area powders of ∼2 times the ALD growth rates on flat substrates.[17,49] These larger growth rates are believed to be
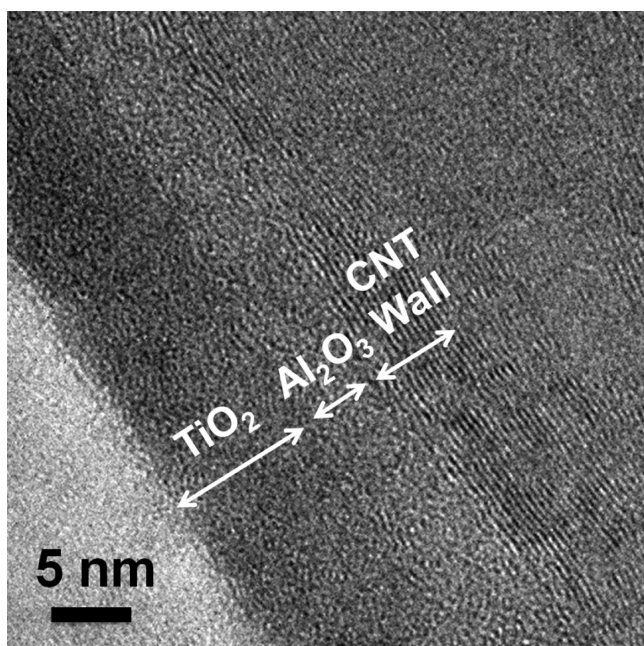
Figure 5. TEM image of CNT after 50 cycles of TiO_2 ALD on the Al_2O_3 adhesion layer on CNT.

Figure 6. Cyclic voltammetry after 50 cycles of TiO_2 ALD on the Al_2O_3 adhesion layer on (a) G and (b) CNT. The potential is defined using an SCE reference electrode.

caused in part by insufficient H_2O purging and the contribution of some chemical vapor deposition (CVD) to the ALD growth.[17,49]

The thickness of ~3.5 nm for the Al_2O_3 layer in Figure 5 is larger than expected for an Al_2O_3 adhesion layer obtained from the NO_2/TMA nucleation treatment and 5 cycles of Al_2O_3 ALD at room temperature.[27] The larger thickness may result from performing the NO_2/TMA nucleation treatment at 180 °C. The original NO_2/TMA nucleation treatment was performed at 25 °C.[27] At 180 °C, NO_2 may react with TMA via a CVD reaction. Thermochemical calculations for the reaction $2Al(CH_3)_3 + 1.5NO_2 \rightarrow Al_2O_3 + 3C_2H_6 + {}^{3}/_{4}N_2$ yield a Gibbs free energy change, ΔG, of approximately −500 kcal per mol of Al_2O_3 at both 25 and 180 °C.[50] This reaction would be spontaneous in the absence of kinetic barriers.

B. Electrochemical Characterization of TiO_2 Films on G and CNT Samples. Figures 6a and 6b show the cyclic voltammetry (CV) curves from 50 cycles of TiO_2 ALD on the Al_2O_3 adhesion layers on G and CNT in 1 M KOH. A typical mass loading of the slurry of 1−2 mg/cm^2 was applied to the nickel foam to prepare the working electrode. The scan rates were varied from 5 to 100 mV/s within the scanning potential window from −0.05 to 0.5 V versus the SCE reference electrode. At a scan rate of 5 mV/s in Figure 6a, the peak oxidation current is observed at 0.39 V during the anodic sweep, and the peak reduction current is observed at 0.30 V during the cathodic sweep.

These redox peaks may result from the transition between TiO_2 and $Ti(OH)_3$ by the reaction $TiO_2 + 2H_2O + e^- \leftrightarrow Ti(OH)_3 + OH^-$.[51−53] The redox peaks may also correspond to the oxidation and reduction reactions of the ions in the electrolyte with the TiO_2 film. One possible reaction is $xK+ + yTiO_2 + e^- \leftrightarrow K_x(TiO_2)_y$. These reactions allow the TiO_2 film to store charge resulting from Faradaic reactions. The electrical double-layer capacitance further enhances the charge storage ability of the TiO_2 ALD-coated composites.
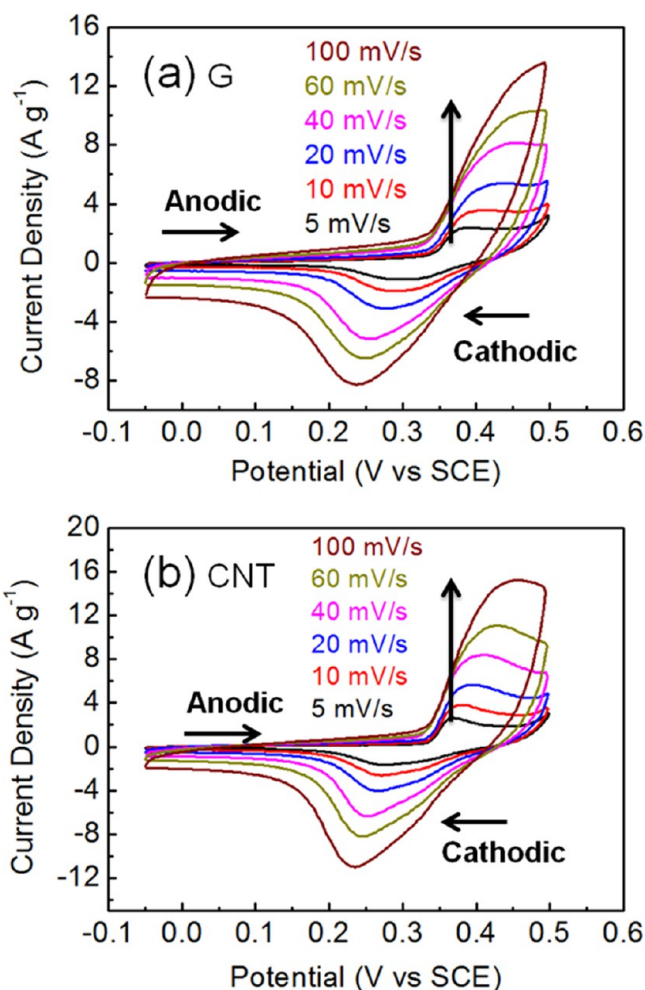
Figures 7a and 7b show the galvanostatic charge/discharge curves at 2 A/g for the TiO_2 ALD-coated G and CNT samples, respectively, after 25 and 50 TiO_2 ALD cycles. The mass in the current density includes the TiO_2, Al_2O_3, and the carbon support. The current density was reversed when the potential reached 0.45 V. These results illustrate that longer times are required for the potential to reach 0.45 V for the samples prepared using 50 TiO_2 ALD cycles. Slightly more than twice the time is required for 50 TiO_2 ALD cycles compared with 25 TiO_2 ALD cycles. These results strongly argue that the charge is being stored in the bulk of the TiO_2 ALD film. The capacitances after 25 and 50 TiO_2 ALD cycles should have been nearly the same if the pseudocapacitance only resulted from surface charge storage.

The results are very similar for the TiO_2 ALD-coated G and CNT samples. This similarity occurs because the experiments were performed at the same current density (A/g) and the G and CNT samples had nearly the same TiO_2 ALD mass loading. These results show that the electrochemical behavior of TiO_2 ALD is equivalent on G and CNT samples. Earlier results demonstrated that charge storage in TiO_2 nanoparticles occurred when the TiO_2 particle size was less than 10 nm.[1] Because pseudocapacitance is derived from the bulk of the TiO_2 film, these earlier results can be interpreted as being caused by the limited electrical conductivity of TiO_2. Charge
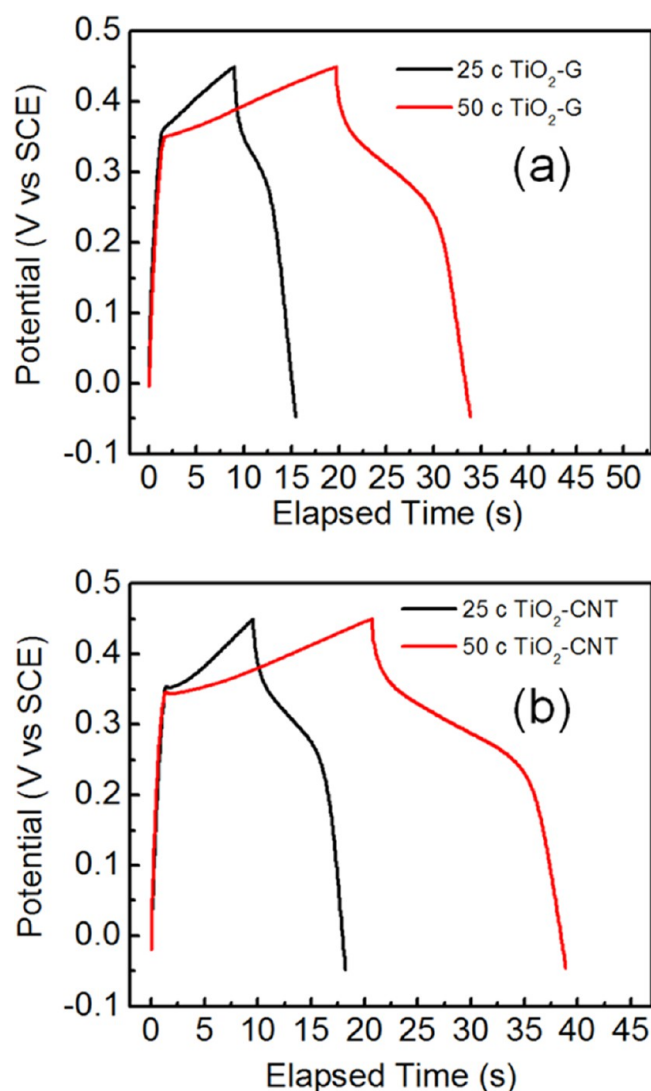
Figure 8. Nyquist plots of G, CNT, and the G and CNT samples after 50 TiO_2 ALD cycles on the Al_2O_3 adhesion layer.

Figure 7. Galvanastatic charge/discharge curves obtained at current density of 2 A/g after 25 and 50 TiO_2 ALD cycles on the Al_2O_3 adhesion layer: (a) G and (b) CNT. The potential is defined using an SCE reference electrode.

storage in the bulk of the TiO_2 nanoparticles was not possible unless electrons could reach the surface of the TiO_2 nanoparticles to allow Faradaic reactions.

Figure 8 shows Nyquist plots from electrochemical impedance spectroscopy of the G, CNT, and TiO_2 ALD-coated G and CNT samples. For each set of data points, the analysis was performed over the frequency range from 0.1 Hz to 100 kHz at an amplitude of 10 mV versus the open circuit potential. Impedance simulations indicate that the CNT sample has the smallest charge transfer resistance at high frequency. The nearly vertical line behavior at low frequency for the CNT sample corresponds closely to an ideal capacitor.[54] The charge transfer and diffusion resistance increase noticeably after 50 TiO_2 ALD cycles. This change indicates slower charge–discharge behavior.[55]

In contrast to the behavior for the CNT samples, the G samples show very similar Nyquist plots. The TiO_2–G composite formed using 50 TiO_2 ALD cycles has nearly identical diffusion and charge transfer resistances as pure graphene. No significant effects on the diffusion and charge
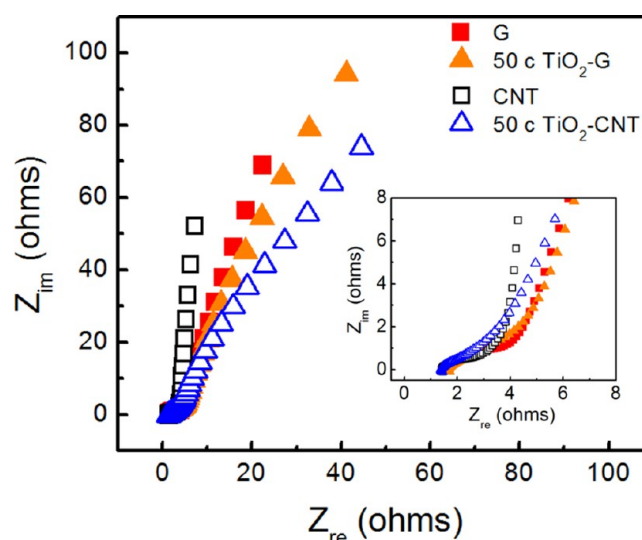
transfer behavior by the ALD coating can be observed for the TiO_2–graphene composite. However, in comparison with CNT, the pure graphene exhibits nonideal capacitor behavior. This nonideal capacitor behavior can be attributed to defects and functional groups existing on the surfaces of the graphene sheets.

Figures 9a and 9b display the total specific capacitances of the G and CNT samples based on calculations from the galvanostatic charge/discharge curves at various current densities. The mass includes the TiO_2, Al_2O_3, and the carbon support. The specific capacitances were derived from $C = I\Delta t/\Delta V$, where I is the current density, Δt is the total discharging time, and ΔV is the voltage range. Figure 9a shows that the highest specific capacitance for the TiO_2–G composite was 97.5 F/g at a current density of 1 A/g. This TiO_2–G composite was fabricated using 50 TiO_2 ALD cycles. Figure 9b shows that the TiO_2–CNT composite fabricated using 50 TiO_2 ALD cycles has the highest specific capacitance of 130.4 F/g at a current density of 1 A/g.

Figure 9 also shows that the specific capacitance is dependent on the number of TiO_2 ALD cycles. At a current density of 1 A/g, the specific capacitance is 47.4 and 97.5 F/g for the 25 and 50 cycles of TiO_2 ALD on G, respectively. The specific capacitance is also 55.8 and 130.4 F/g for the 25 and 50 cycles of TiO_2 ALD on CNT, respectively. This behavior again indicates that the pseudocapacitance does not result only from the surface of the TiO_2 ALD film. A significant fraction of the specific capacitance results from the bulk of the TiO_2 ALD film.

The results in Figure 9 can be used to estimate the molar ratio of stored charge to TiO_2 after a charging voltage of 0.45 V. The molar ratio of stored charge to TiO_2 can be determined from the specific capacitances at a current density of 1 A/g. This determination employs the wt % of TiO_2, Al_2O_3, and G or CNT in the various samples. This estimate assumes that the G and CNT contribute equally to the specific capacitance before and after the TiO_2 ALD on the Al_2O_3 adhesion layer.

The molar ratios of stored charge to TiO_2 are 0.027 and 0.055 (mol charge/mol TiO_2) for the 25 and 50 cycles of TiO_2 ALD on G, respectively. The molar ratios of stored charge to TiO_2 are 0.035 and 0.077 for the 25 and 50 cycles of TiO_2 ALD on CNT, respectively. The stored charge could result from
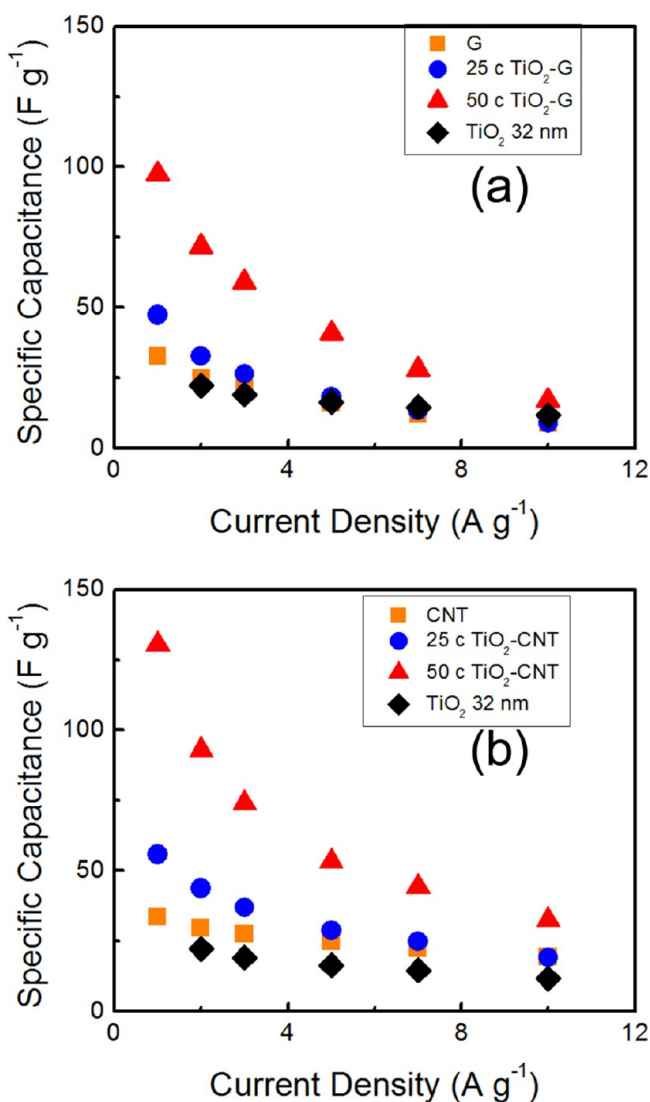
Figure 9. Specific capacitance of the commercial TiO_2 nanoparticles, the G and CNT samples and the samples after 25 and 50 TiO_2 ALD cycles on the Al_2O_3 adhesion layer: (a) G and (b) CNT.

either $TiO_2 + 2H_2O + e^- \leftrightarrow Ti(OH)_3 + OH^-$ or $xK + yTiO_2 + e^- \leftrightarrow K_x(TiO_2)_y$. If the charge is stored in $K_x(TiO_2)_y$, then the molar ratios of stored charge to TiO_2 are comparable with the molar ratios observed for solid solutions of alkali metals, such as Li, in TiO_2.[56]

Although Figure 7 suggests that the stored charge is linearly dependent on the number TiO_2 ALD cycles, the molar ratios of stored charge to TiO_2 are higher for the thicker TiO_2 ALD films. The higher molar ratios of stored charge to TiO_2 result from the TGA measurements that indicate that the TiO_2 mass is not linear with the number of TiO_2 ALD cycles. The TGA measurements reveal that more TiO_2 mass is deposited in the first 25 TiO_2 ALD cycles compared with the second 25 TiO_2 ALD cycles. The TiO_2 mass deposited during the first 25 TiO_2 ALD cycles could be larger because of nucleation effects on the Al_2O_3 adhesion layer. For example, the Al_2O_3 ALD surface has a high hydroxyl coverage that may allow for more TiO_2 deposition during the initial TiO_2 ALD cycles.[57]

The ability of the TiO_2 ALD film to store charge may also change with thickness. The charge storage ability will depend on ion transport rates in the film that will vary with film thickness.[58] The charge storage ability may also be dependent on the evolving morphology or structure of the film with thickness. If the TiO_2 ALD film has a higher surface roughness after 50 cycles of TiO_2 ALD, then the higher surface roughness could adsorb more H^+ or K^+ ions. The surface charge adsorption would add to the bulk charge absorption. If the TiO_2 ALD film has a more amorphous structure after 50 cycles of TiO_2 ALD, then the more amorphous structure could also store more charge.[59,60]

The electrochemical performance of the TiO_2 ALD-coated G and CNT samples is also compared with uncoated G and CNT samples and P25 TiO_2 nanoparticles with a particle size of 32 nm and the surface area of 45 m^2/g. The P25 TiO_2 nanoparticles were obtained from Sigma-Aldrich. The uncoated G and CNT samples have capacitances of 32 F/g and 34 F/g, respectively, at 1 A/g. These capacitances are derived from pristine, unfunctionalized G and CNT samples and are much lower than the TiO_2 ALD-coated samples. A lower capacitance of 25 F/g was obtained for the pure TiO_2 nanoparticles.

The specific capacitance results for the TiO_2 ALD-coatings on the Al_2O_3 adhesion layers on G in Figure 9a can also be compared with our earlier results for TiO_2 ALD on G without the Al_2O_3 adhesion layer.[5] The amorphous TiO_2 ALD films on the Al_2O_3 adhesion layer have a specific capacitance that is similar to the specific capacitance of the crystalline TiO_2 nanoparticles deposited by TiO_2 ALD without the Al_2O_3 adhesion layer after the same number of TiO_2 ALD cycles. The highest specific capacitance for the amorphous TiO_2-G composite fabricated using 50 TiO_2 ALD cycles was 97.5 F/g at a current density of 1 A/g and 72.7 F/g at 10 mV/s. The highest specific capacitance for the crystalline TiO_2 nanoparticles on G fabricated using 50 TiO_2 ALD cycles was 75 F/g at a scan rate of 10 mV/s.[5]

The TiO_2 ALD-coated samples also display excellent cycle stability. Figure 10 shows the cycle stability of CNT and TiO_2-ALD coated CNT samples at 2 A/g. Both the CNT and TiO_2-ALD coated CNT samples show capacitance retention that initially increases with cycle number. This behavior may be caused by the initial activation of the porous electrode. Both CNT and the TiO_2 ALD-coated CNT sample show ~100% retention after 1000 charge/discharge cycles. This exceptional stability is attributed to the strong chemical linkage between TiO_2 and the Al_2O_3 adhesion layer on the TiO_2 ALD-coated CNT samples.[5]

C. Electrochemical Characterization of Asymmetric and Symmetric Cells. Electrochemical tests were also conducted on asymmetric cells based on TiO_2 ALD-coated G and CNT electrodes. These asymmetric cells were compared with symmetric cells based on CNT electrodes. Symmetric supercapacitor cells suffer from a low operating voltage in aqueous solution because of the limits of water decomposition at high potential.[61] The asymmetric cell may display enhanced performance because the extra charge storage resulting from the pseudocapacitance of TiO_2 should lead to an increase in energy density.[55,62,63] In addition, the utilization of the different potential windows for the cathode and anode may expand the operation voltage of the asymmetric cell. A similar strategy has been employed based on TiO_2-coated activated carbon composites and TiO_2 nanotubes as the negative anode electrode in asymmetric capacitors.[64,65]

As shown by the CV results in Figure 11a, the CNT electrode exhibits a stable voltage window between −1 and 0 V. In comparison, the TiO_2 ALD-coated CNT electrode is stable
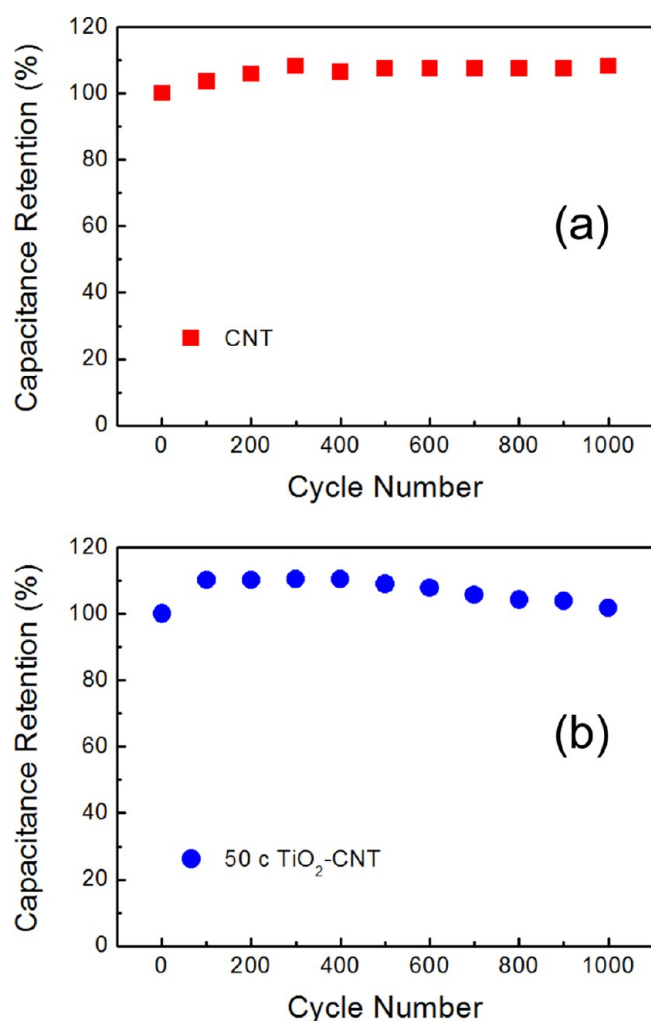
22503

dx.doi.org/10.1021/jp4066955 | J. Phys. Chem. C 2013, 117, 22497−22508

Figure 10. Capacitance retention versus charge/discharge cycle number at 2 A/g for (a) CNT and (b) after 50 TiO$_2$ ALD cycles on the Al$_2$O$_3$ adhesion layer on CNT.

Figure 11. (a) Cyclic voltammetry (CV) of the CNT electrode and the TiO$_2$−CNT electrode after 50 TiO$_2$ ALD cycles on the Al$_2$O$_3$ adhesion layer on CNT. (b) CV of an asymmetric cell defined by a CNT electrode and a TiO$_2$−CNT electrode after 50 TiO$_2$ ALD cycles on the Al$_2$O$_3$ adhesion layer on CNT. The CV measurements were performed in a three-electrode cell at a scan rate of 10 mV/s.

between −0.05 and 0.5 V. Consequently, the asymmetric cell constructed from these two electrodes should have a stable operation window of 1.5 V. The TiO$_2$ ALD-coated CNT electrode coated using 50 TiO$_2$ ALD cycles was employed as the positive cathode electrode. The uncoated CNT electrode was employed as the negative anode electrode.

In an asymmetric cell, the charge stored in the cathode is balanced by an equivalent amount of charge stored in the anode. The optimized mass ratio of the TiO$_2$ ALD-coated CNT positive electrode using 50 cycles of TiO$_2$ ALD to the uncoated CNT negative electrode is 0.66. This mass ratio is based on the equation $q = Cm\Delta E$, where q is the charge stored on each electrode, ΔE is the potential range, m is the mass of each electrode, and C is the specific capacitance. Figure 11b shows the CV curve of the asymmetric cell with an optimized cathode/anode mass ratio of 0.66 in 1 M KOH at a scan rate of 10 mV/s. The asymmetric cell shows good current−voltage response over a stable potential window of 1.5 V.

Figure 12a summarizes the specific capacitance of the asymmetric cell at various scan rates. The specific capacitances were calculated from the CV curves based on $C = \int I \, dt / m\Delta V$, where I is the current, dt is the scan time interval, m is the sample mass, and ΔV is the voltage range of each scan. This capacitance accounts for the total mass of both anode and
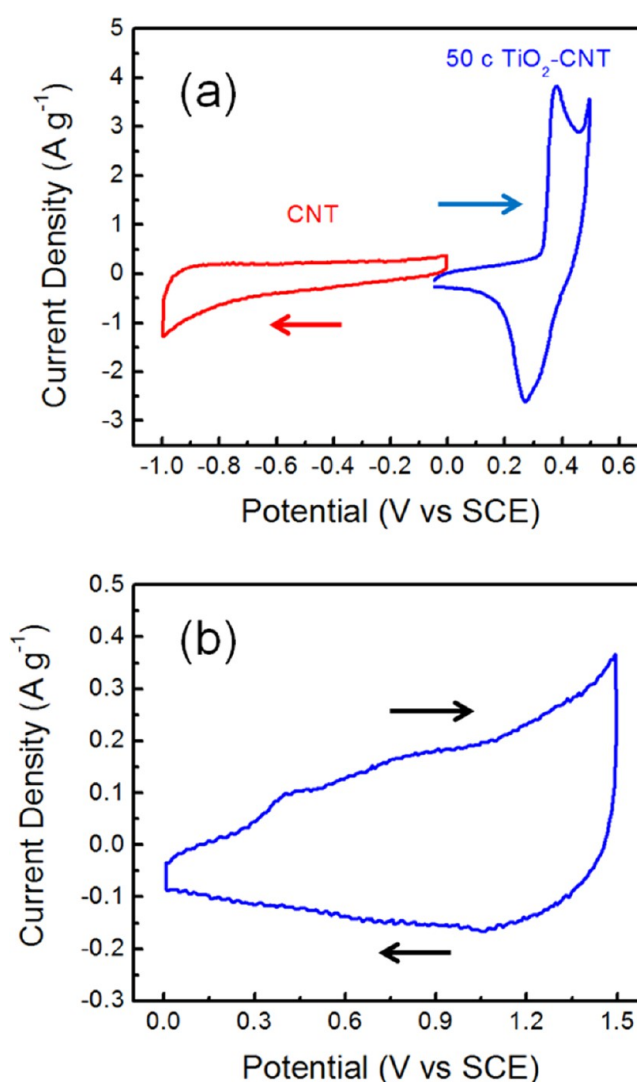
cathode materials. The CNT symmetric cell and asymmetric cell using TiO$_2$ ALD-coated CNT after 25 cycle TiO$_2$ ALD cycles are also displayed for comparison.

Figure 12a shows that the specific capacitance at a scan rate of 5 mV/s increases significantly from 6.1 F/g for the CNT symmetric cell to 14.3 F/g for the asymmetric cell formed using the TiO$_2$ ALD-coated CNT electrode after 50 TiO$_2$ ALD cycles and the uncoated CNT electrode. The asymmetric cell formed using the TiO$_2$ ALD-coated CNT electrode after 25 TiO$_2$ ALD cycles has a specific capacitance of 10.2 F/g at a scan rate of 5 mV/s. Increases in the specific capacitance were also observed in the previous work on asymmetric capacitors using TiO$_2$.[64,65] The specific capacitance of the asymmetric cell gradually decreases at higher scan rates. This decrease is attributed to diffusion limitations in bulk TiO$_2$. In contrast, the electric double layer storage mechanism enables the symmetric CNT cell to maintain an excellent rate capability regardless of the scan rate.
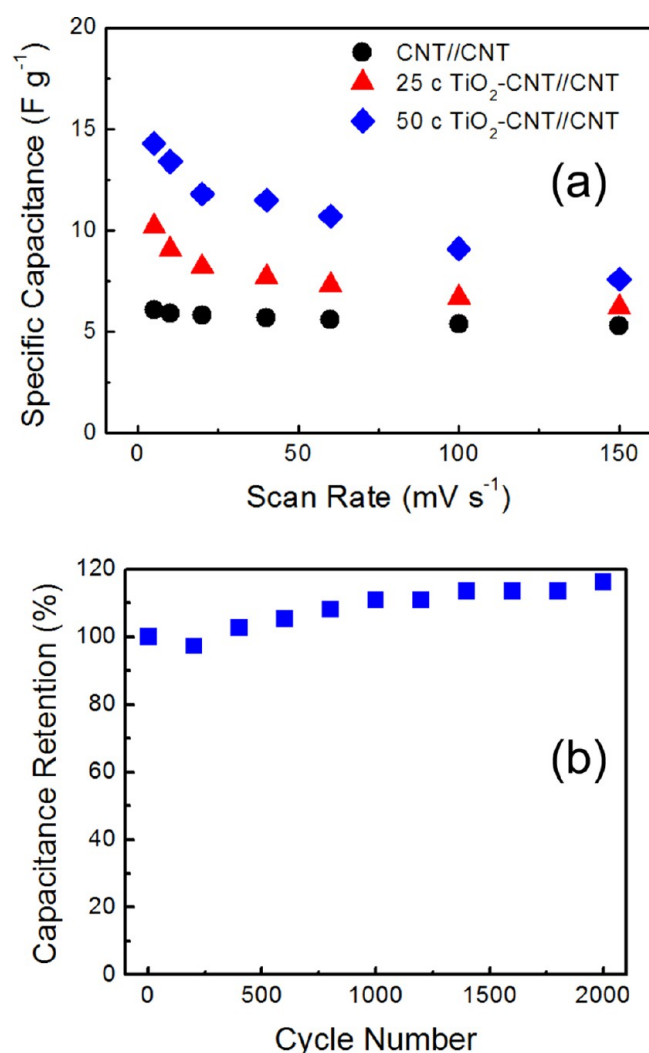
Figure 13. Ragone plots of the CNT symmetric cell and asymmetric cell defined by a CNT electrode and a TiO_2–CNT electrode after 50 TiO_2 ALD cycles on the Al_2O_3 adhesion layer on CNT.

Figure 12. (a) Specific capacitances of CNT symmetric cell and asymmetric cell defined by a CNT electrode and a TiO_2–CNT electrode after 50 TiO_2 ALD cycles on the Al_2O_3 adhesion layer on CNT. (b) Cycle stability of asymmetric cell defined by a CNT electrode and a TiO_2–CNT electrode after 50 TiO_2 ALD cycles on the Al_2O_3 adhesion layer on CNT.

The asymmetric cell formed by the TiO_2 ALD-coated CNT electrode after 50 TiO_2 ALD cycles also displays excellent cycling stability. Figure 12b shows that no decay was observed in the capacitance of this asymmetric cell after 2000 cycles. This cycling performance is better than typical asymmetric supercapacitors.[62] This stability enhancement is attributed to the chemical stability of TiO_2 and the strong anchoring of the TiO_2 ALD layer on the CNT substrate. Similar stability was also observed for TiO_2 asymmetric capacitors based on TiO_2 and carbon counter electrodes.[64,65]

The higher operating potential window of the asymmetric cell also provides extra advantages for improving energy and power densities. Ragone plots of the asymmetric and symmetric cells are shown in Figure 13. The asymmetric CNT cell exhibits much higher energy and power density than the symmetric CNT cell. A high energy density of 4.47 W·h/kg is achieved for the asymmetric cell containing the TiO_2 ALD-coated CNT electrode after 50 TiO_2 ALD cycles. This energy density is ~4 times higher than the energy density of the CNT symmetric
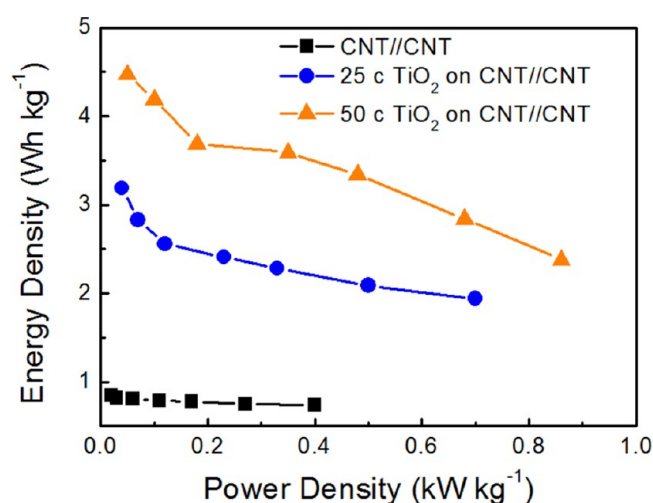
cell. Note that the energy and power densities shown in the Ragone plots are based on the total mass of the active materials.

The comparison shown in Figure 13 demonstrates the performance improvement of the asymmetric cell. The performance can be improved further by depositing other metal oxides with higher pseudocapacitance such as MnO_2, V_2O_5, and NiO on the CNT substrates. From this study, TiO_2 has a relatively low measured specific capacitance of 25 F/g for TiO_2 nanoparticles. A larger specific capacitance of ~100−130 F/g is observed for TiO_2 composites with G and CNT. Earlier studies have also reported a pseudocapacitance of ~18 F/g for carbon titania mesoporous composite whiskers.[66] In comparison, MnO_2, V_2O_5, and NiO have much higher reported measured pseudocapacitances of >1000 F/g.[67−69] ALD can deposit these various metal oxides that should produce higher energy densities than the energy density obtained using TiO_2 ALD.

IV. CONCLUSIONS

Pseudocapacitance supercapacitors were fabricated by depositing amorphous TiO_2 ALD thin films onto the surface of both G and CNT samples. An ultrathin Al_2O_3 adhesion layer was employed to obtain the conformal and amorphous TiO_2 ALD films. The electrochemical characteristics of TiO_2 ALD films in 1 M KOH electrolyte were then determined using a variety of techniques including cyclic voltammetry, galvanostatic charge/discharge curves, and electrochemical impedance spectroscopy. The relatively low electrical conductivity and ionic diffusivity of TiO_2 did not limit these measurements because the TiO_2 ALD films were ultrathin.

The pseudocapacitance of the TiO_2 ALD films greatly exceeded the electric double layer capacitance of the uncoated G and CNT samples. The measurements determined that the specific capacitances of the TiO_2 ALD-coated G and CNT samples were 97.5 and 135 F/g, respectively, after 50 TiO_2 ALD cycles at 1 A/g. Additional galvanostatic charge/discharge experiments revealed that the charge storage was dependent on the TiO_2 ALD film thickness. This dependence on TiO_2 ALD film thickness argues that the pseudocapacitance is derived largely from the TiO_2 bulk and is not limited to the TiO_2 ALD surface. Estimates of the molar ratio of stored charge to TiO_2

were in the range of 0.03−0.08 for the various TiO$_2$ ALD-coated G and CNT samples.

An asymmetric cell was also developed based on TiO$_2$ ALD-coated CNT samples as the positive electrode and uncoated CNT samples as the negative electrode. This energy storage device could be reversibly operated over a wide voltage range of 0−1.5 V in aqueous electrolyte. A high energy density of 4.47 W·h/kg was achieved on the basis of the total weight of both electrodes. This energy density was ∼4 times higher than the symmetric CNT cell. The TiO$_2$ ALD-coated G and CNT electrodes and the asymmetric cell based on the TiO$_2$ ALD-coated electrode also exhibited excellent stability over >1000 cycles.

The results of this study demonstrate that metal oxide ALD on high surface area conducting substrates can be used to fabricate high energy storage supercapacitors. Although the current results based on TiO$_2$ ALD are promising, specific capacitances are expected to be higher using other metal oxides with higher pseudocapacitance values than TiO$_2$ such as MnO$_2$, V$_2$O$_5$, and NiO. The combination of metal oxide ALD on high surface area conducting G and CNT substrates is a very promising strategy for fabricating high energy storage pseudocapacitance supercapacitors.

■ AUTHOR INFORMATION

Corresponding Authors
*E-mail Steven.George@Colorado.edu; Ph 303-492-3398 (S.M.G.).
*E-mail lianj@rpi.edu; Ph 518-276-6081 (J.L.).

Notes
The authors declare no competing financial interest.

■ ACKNOWLEDGMENTS

■ REFERENCES

(1) Wang, J.; Polleux, J.; Lim, J.; Dunn, B. Pseudocapacitive Contributions to Electrochemical Energy Storage in TiO$_2$ (Anatase) Nanoparticles. *J. Phys. Chem. C* **2007**, *111*, 14925−14931.

(2) Ban, C. M.; Xie, M.; Sun, X.; Travis, J. J.; Wang, G. W.; Sun, H. T.; Dillon, A. C.; Lian, J.; George, S. M. ALD of Amorphous TiO$_2$ on an Al$_2$O$_3$ Adhesion Layer on Graphene as an Anode for Li Ion Batteries. *Nanotechnology* **2013**, *24*, 424002.

(3) Chen, J. S.; Tan, Y. L.; Li, C. M.; Cheah, Y. L.; Luan, D. Y.; Madhavi, S.; Boey, F. Y. C.; Archer, L. A.; Lou, X. W. Constructing Hierarchical Spheres from Large Ultrathin Anatase TiO$_2$ Nanosheets with Nearly 100% Exposed (001) Facets for Fast Reversible Lithium Storage. *J. Am. Chem. Soc.* **2010**, *132*, 6124−6130.

(4) Lin, Y. M.; Abel, P. R.; Flaherty, D. W.; Wu, J.; Stevenson, K. J.; Heller, A.; Mullins, C. B. Morphology Dependence of the Lithium Storage Capability and Rate Performance of Amorphous TiO$_2$ Electrodes. *J. Phys. Chem. C* **2011**, *115*, 2585−2591.

(5) Sun, X.; Xie, M.; Wang, G.; Sun, H.; Cavanagh, A. S.; Travis, J. J.; George, S. M.; Lian, J. Atomic Layer Deposition of TiO$_2$ on Graphene for Supercapacitors. *J. Electrochem. Soc.* **2012**, *159*, A364−A369.

(6) Brezesinski, T.; Wang, J.; Polleux, J.; Dunn, B.; Tolbert, S. H. Templated Nanocrystal-Based Porous TiO$_2$ Films for Next-Generation Electrochemical Capacitors. *J. Am. Chem. Soc.* **2009**, *131*, 1802−1809.

(7) Breckenridge, R. G.; Hosler, W. R. Electrical Properties of Titanium Dioxide Semiconductors. *Phys. Rev.* **1953**, *91*, 793−802.

(8) Akalework, N. G.; Pan, C. J.; Su, W. N.; Rick, J.; Tsai, M. C.; Lee, J. F.; Lin, J. M.; Tsai, L. D.; Hwang, B. J. Ultrathin TiO$_2$-Coated MWCNTs with Excellent Conductivity and SMSI Nature as Pt Catalyst Support for Oxygen Reduction Reaction in PEMFCs. *J. Mater. Chem.* **2012**, *22*, 20977−20985.

(9) Reddy, A. L. M.; Ramaprabhu, S. Nanocrystalline Metal Oxides Dispersed Multiwalled Carbon Nanotubes as Supercapacitor Electrodes. *J. Phys. Chem. C* **2007**, *111*, 7727−7734.

(10) Hou, J. B.; Shao, Y. Y.; Ellis, M. W.; Moore, R. B.; Yi, B. L. Graphene-Based Electrochemical Energy Conversion and Storage: Fuel Cells, Supercapacitors and Lithium Ion Batteries. *Phys. Chem. Chem. Phys.* **2011**, *13*, 15384−15402.

(11) Simon, P.; Gogotsi, Y. Materials for Electrochemical Capacitors. *Nat. Mater.* **2008**, *7*, 845−854.

(12) Wu, Z. S.; Zhou, G. M.; Yin, L. C.; Ren, W.; Li, F.; Cheng, H. M. Graphene/Metal Oxide Composite Electrode Materials for Energy Storage. *Nano Energy* **2012**, *1*, 107−131.

(13) Zhi, M. J.; Xiang, C. C.; Li, J. T.; Li, M.; Wu, N. Q. Nanostructured Carbon-Metal Oxide Composite Electrodes for Supercapacitors: A Review. *Nanoscale* **2013**, *5*, 72−88.

(14) George, S. M. Atomic Layer Deposition: An Overview. *Chem. Rev.* **2010**, *110*, 111−131.

(15) Elam, J. W.; Routkevitch, D.; Mardilovich, P. P.; George, S. M. Conformal Coating on Ultrahigh-Aspect-Ratio Nanopores of Anodic Alumina by Atomic Layer Deposition. *Chem. Mater.* **2003**, *15*, 3507−3517.

(16) Gordon, R. G.; Hausmann, D.; Kim, E.; Shepard, J. A Kinetic Model for Step Coverage by Atomic Layer Deposition in Narrow Holes or Trenches. *Chem. Vap. Deposition* **2003**, *9*, 73−78.

(17) McCormick, J. A.; Rice, K. P.; Paul, D. F.; Weimer, A. W.; George, S. M. Analysis of Al$_2$O$_3$ Atomic Layer Deposition on ZrO$_2$ Nanoparticles in a Rotary Reactor. *Chem. Vap. Deposition* **2007**, *13*, 491−498.

(18) Ferguson, J. D.; Weimer, A. W.; George, S. M. Atomic Layer Deposition of Ultrathin and Conformal Al$_2$O$_3$ Films on BN Particles. *Thin Solid Films* **2000**, *371*, 95−104.

(19) Liu, J. H.; Chen, J. S.; Wei, X. F.; Lou, X. W.; Liu, X. W. Sandwich-Like, Stacked Ultrathin Titanate Nanosheets for Ultrafast Lithium Storage. *Adv. Mater.* **2011**, *23*, 998−1002.

(20) Wang, D. H.; Choi, D. W.; Li, J.; Yang, Z. G.; Nie, Z. M.; Kou, R.; Hu, D. H.; Wang, C. M.; Saraf, L. V.; Zhang, J. G.; et al. Self-Assembled TiO$_2$ Graphene Hybrid Nanostructures for Enhanced Li-Ion Insertion. *ACS Nano* **2009**, *3*, 907−914.

(21) Li, N.; Liu, G.; Zhen, C.; Li, F.; Zhang, L. L.; Cheng, H. M. Battery Performance and Photocatalytic Activity of Mesoporous Anatase TiO$_2$ Nanospheres/Graphene Composites by Template-Free Self-Assembly. *Adv. Funct. Mater.* **2011**, *21*, 1717−1722.

(22) McCormick, J. A.; Cloutier, B. L.; Weimer, A. W.; George, S. M. Rotary Reactor for Atomic Layer Deposition on Large Quantities of Nanoparticles. *J. Vac. Sci. Technol., A* **2007**, *25*, 67−74.

(23) Cavanagh, A. S.; Wilson, C. A.; Weimer, A. W.; George, S. M. Atomic Layer Deposition on Gram Quantities of Multi-walled Carbon Nanotubes. *Nanotechnology* **2009**, *20*, 255602.

(24) Hummers, W. S.; Offeman, R. E. Preparation of Graphitic Oxide. *J. Am. Chem. Soc.* **1958**, *80*, 1339−1339.

(25) McAllister, M. J.; Li, J. L.; Adamson, D. H.; Schniepp, H. C.; Abdala, A. A.; Liu, J.; Herrera-Alonso, M.; Milius, D. L.; Car, R.; Prud'homme, R. K.; Aksay, I. A. Single Sheet Functionalized Graphene by Oxidation and Thermal Expansion of Graphite. *Chem. Mater.* **2007**, *19*, 4396−4404.

(26) Wang, G.; Sun, X.; Lu, F.; Yu, Q.; Liu, C.; Lian, J. Controlled Synthesis of MnSn(OH)$_6$/Graphene Nanocomposites and their Electrochemical Properties as Capacitive Materials. *J. Solid State Chem.* **2012**, *185*, 172−179.

(27) Farmer, D. B.; Gordon, R. G. Atomic Layer Deposition on Suspended Single-Walled Carbon Nanotubes via Gas-Phase Noncovalent Functionalization. *Nano Lett.* **2006**, *6*, 699−703.

(28) Dillon, A. C.; Ott, A. W.; Way, J. D.; George, S. M. Surface Chemistry of Al_2O_3 Deposition using $Al(CH_3)_3$ and H_2O in a Binary Reaction Sequence. *Surf. Sci.* **1995**, *322*, 230−242.

(29) Elam, J. W.; Groner, M. D.; George, S. M. Viscous Flow Reactor with Quartz Crystal Microbalance for Thin Film Growth by Atomic Layer Deposition. *Rev. Sci. Instrum.* **2002**, *73*, 2981−2987.

(30) Groner, M. D.; Fabreguette, F. H.; Elam, J. W.; George, S. M. Low-Temperature Al_2O_3 Atomic Layer Deposition. *Chem. Mater.* **2004**, *16*, 639−645.

(31) Ott, A. W.; Klaus, J. W.; Johnson, J. M.; George, S. M. Al_2O_3 Thin Film Growth on Si(100) Using Binary Reaction Sequence Chemistry. *Thin Solid Films* **1997**, *292*, 135−144.

(32) Ritala, M.; Leskela, M.; Nykanen, E.; Soininen, P.; Niinisto, L. Growth of Titanium-Dioxide Thin Films by Atomic Layer Epitaxy. *Thin Solid Films* **1993**, *225*, 288−295.

(33) Wang, G. X.; Yang, J.; Park, J.; Gou, X. L.; Wang, B.; Liu, H.; Yao, J. Facile Synthesis and Characterization of Graphene Nanosheets. *J. Phys. Chem. C* **2008**, *112*, 8192−8195.

(34) Wu, Z. S.; Ren, W. C.; Wen, L.; Gao, L. B.; Zhao, J. P.; Chen, Z. P.; Zhou, G. M.; Li, F.; Cheng, H. M. Graphene Anchored with Co_3O_4 Nanoparticles as Anode of Lithium Ion Batteries with Enhanced Reversible Capacity and Cyclic Performance. *ACS Nano* **2010**, *4*, 3187−3194.

(35) Wang, G.; Sun, X.; Lu, F.; Sun, H.; Yu, M.; Jiang, W.; Liu, C.; Lian, J. Flexible Pillared Graphene-Paper Electrodes for High-Performance Electrochemical Supercapacitors. *Small* **2012**, *8*, 452−459.

(36) Li, W. Z.; Liang, C. H.; Zhou, W. J.; Qiu, J. S.; Zhou, Z. H.; Sun, G. Q.; Xin, Q. Preparation and Characterization of Multiwalled Carbon Nanotube-Supported Platinum for Cathode Catalysts of Direct Methanol Fuel Cells. *J. Phys. Chem. B* **2003**, *107*, 6292−6299.

(37) Aarik, J.; Aidla, A.; Kiisler, A.-A.; Uustare, T.; Sammelselg, V. Effect of Crystal Structure on Optical Properties of TiO_2 Films Grown by Atomic Layer Deposition. *Thin Solid Films* **1997**, *305*, 270−273.

(38) Jayashree, R. S.; Kamath, P. V.; Subbanna, G. N. The Effect of Crystallinity on the Reversible Discharge Capacity of Nickel Hydroxide. *J. Electrochem. Soc.* **2000**, *147*, 2029−2032.

(39) Sun, X.; Wang, G. K.; Hwang, J. Y.; Lian, J. Porous Nickel Oxide Nano-Sheets for High Performance Pseudocapacitance Materials. *J. Mater. Chem.* **2011**, *21*, 16581−16588.

(40) Lee, H. Y.; Goodenough, J. B. Supercapacitor Behavior with KCl Electrolyte. *J. Solid State Chem.* **1999**, *144*, 220−223.

(41) Lee, H. Y.; Goodenough, J. B. Ideal Supercapacitor Behavior of Amorphous $V_2O_5 \cdot nH_2O$ in Potassium Chloride (KCl) Aqueous Solution. *J. Solid State Chem.* **1999**, *148*, 81−84.

(42) Fang, H. T.; Liu, M.; Wang, D. W.; Sun, T.; Guan, D. S.; Li, F.; Zhou, J. G.; Sham, T. K.; Cheng, H. M. Comparison of the Rate Capability of Nanostructured Amorphous and Anatase TiO_2 for Lithium Insertion Using Anodic TiO_2 Nanotube Arrays. *Nanotechnology* **2009**, *20*, 225701.

(43) Yan, X. B.; Tay, B. K.; Yang, Y. Dispersing and Functionalizing Multiwalled Carbon Nanotubes in TiO_2 Sol. *J. Phys. Chem. B* **2006**, *110*, 25844−25849.

(44) An, G. M.; Ma, W. H.; Sun, Z. Y.; Liu, Z. M.; Han, B. X.; Miao, S. D.; Miao, Z. J.; Ding, K. L. Preparation of Titania/Carbon Nanotube Composites using Supercritical Ethanol and their Photocatalytic Activity for Phenol Degradation under Visible Light Irradiation. *Carbon* **2007**, *45*, 1795−1801.

(45) Huang, B. S.; Tseng, H. H.; Wey, M. Y. Comparison of Visible-Light-Driven Routes of Anion-Doped TiO_2 and Composite Photocatalyst. *J. Ceram. Soc. Jpn.* **2009**, *117*, 753−758.

(46) Borghols, W. J. H.; Lutzenkirchen-Hecht, D.; Haake, U.; Chan, W.; Lafont, U.; Kelder, E. M.; van Eck, E. R. H.; Kentgens, A. P. M.; Mulder, F. M.; Wagemaker, M. Lithium Storage in Amorphous TiO_2 Nanoparticles. *J. Electrochem. Soc.* **2010**, *157*, A582−A588.

(47) Liu, Y.; Qian, W. Z.; Zhang, Q.; Ning, G. Q.; Luo, G. H.; Wang, Y.; Wang, D. Z.; Wei, F. Synthesis of High-Quality, Double-Walled Carbon Nanotubes in a Fluidized Bed Reactor. *Chem. Eng. Technol.* **2009**, *32*, 73−79.

(48) Groner, M. D.; Elam, J. W.; Fabreguette, F. H.; George, S. M. Electrical Characterization of Thin Al_2O_3 Films Grown by Atomic Layer Deposition on Silicon and Various Metal Substrates. *Thin Solid Films* **2002**, *413*, 186−197.

(49) Ferguson, J. D.; Weimer, A. W.; George, S. M. Atomic Layer Deposition of Al_2O_3 Films on Polyethylene Particles. *Chem. Mater.* **2004**, *16*, 5602−5609.

(50) *HSC Chemistry*, 5.11 ed.; Outokumpu Research Oy: Pori, Finland.

(51) Cao, L.; Xu, F.; Liang, Y. Y.; Li, H. L. Preparation of the Novel Nanocomposite $Co(OH)_2$/Ultra-Stable Y Zeolite and Its Application as a Supercapacitor with High Energy Density. *Adv. Mater.* **2004**, *16*, 1853−1857.

(52) Huang, Q. H.; Wang, X. Y.; Li, J.; Dai, C. L.; Gamboa, S.; Sebastian, P. J. Nickel Hydroxide/Activated Carbon Composite Electrodes for Electrochemical Capacitors. *J. Power Sources* **2007**, *164*, 425−429.

(53) Schweitzer, G. K.; Pesterfield, L. L. *The Aqueous Chemistry of the Elements*; Oxford University Press: New York, 2010.

(54) Stoller, M. D.; Park, S. J.; Zhu, Y. W.; An, J. H.; Ruoff, R. S. Graphene-Based Ultracapacitors. *Nano Lett.* **2008**, *8*, 3498−3502.

(55) Wang, Q.; Wen, Z. H.; Li, J. H. A Hybrid Supercapacitor Fabricated with a Carbon Nanotube Cathode and a TiO_2-B Nanowire Anode. *Adv. Funct. Mater.* **2006**, *16*, 2141−2146.

(56) Wagemaker, M.; Borghols, W. J. H.; Mulder, F. M. Large Impact of Particle Size on Insertion Reactions. A Case for Anatase Li_xTiO_2. *J. Am. Chem. Soc.* **2007**, *129*, 4323−4327.

(57) Cameron, M. A.; Gartland, I. P.; Smith, J. A.; Diaz, S. F.; George, S. M. Atomic Layer Deposition of SiO_2 and TiO_2 in Alumina Tubular Membranes: Pore Reduction and Effect of Surface Species on Gas Transport. *Langmuir* **2000**, *16*, 7435−7444.

(58) Zhang, H.; Cao, G. P.; Wang, Z. Y.; Yang, Y. S.; Shi, Z. J.; Gu, Z. N. Growth of Manganese Oxide Nanoflowers on Vertically-Aligned Carbon Nanotube Arrays for High-Rate Electrochemical Capacitive Energy Storage. *Nano Lett.* **2008**, *8*, 2664−2668.

(59) Reddy, R. N.; Reddy, R. G. Synthesis and Electrochemical Characterization of Amorphous MnO_2 Electrochemical Capacitor Electrode Material. *J. Power Sources* **2004**, *132*, 315−320.

(60) Zheng, J. P.; Jow, T. R. A New Charge Storage Mechanism for Electrochemical Capacitors. *J. Electrochem. Soc.* **1995**, *142*, L6−L8.

(61) Liu, C.; Li, F.; Ma, L. P.; Cheng, H. M. Advanced Materials for Energy Storage. *Adv. Mater.* **2010**, *22*, E28−E62.

(62) Wu, Z. S.; Ren, W. C.; Wang, D. W.; Li, F.; Liu, B. L.; Cheng, H. M. High-Energy MnO_2 Nanowire/Graphene and Graphene Asymmetric Electrochemical Capacitors. *ACS Nano* **2010**, *4*, 5835−5842.

(63) Fan, Z. J.; Yan, J.; Wei, T.; Zhi, L. J.; Ning, G. Q.; Li, T. Y.; Wei, F. Asymmetric Supercapacitors Based on Graphene/MnO_2 and Activated Carbon Nanofiber Electrodes with High Power and Energy Density. *Adv. Funct. Mater.* **2011**, *21*, 2366−2375.

(64) Kim, S. O.; Lee, J. K. Nanostructured TiO_2-Coated Activated Carbon Composite as an Electrode Material for Asymmetric Hybrid Capacitors. *J. Nanosci. Nanotechnol.* **2012**, *12*, 1292−1295.

(65) Wang, Q.; Wen, Z. H.; Li, J. H. Carbon Nanotubes/TiO_2 Nanotubes Hybrid Supercapacitor. *J. Nanosci. Nanotechnol.* **2007**, *7*, 3328−3331.

(66) Lu, L. H.; Zhu, Y. D.; Li, F. J.; Zhuang, W.; Chan, K. Y.; Lu, X. H. Carbon Titania Mesoporous Composite Whisker as Stable Supercapacitor Electrode Material. *J. Mater. Chem.* **2010**, *20*, 7645−7651.

(67) Boukhalfa, S.; Evanoff, K.; Yushin, G. Atomic Layer Deposition of Vanadium Oxide on Carbon Nanotubes for High-Power Supercapacitor Electrodes. *Energy Environ. Sci.* **2012**, *5*, 6872−6879.

(68) Lang, X. Y.; Hirata, A.; Fujita, T.; Chen, M. W. Nanoporous Metal/Oxide Hybrid Electrodes for Electrochemical Supercapacitors. *Nat. Nanotechnol.* **2011**, *6*, 232−236.

(69) Lu, Q.; Lattanzi, M. W.; Chen, Y. P.; Kou, X. M.; Li, W. F.; Fan, X.; Unruh, K. M.; Chen, J. G. G.; Xiao, J. Q. Supercapacitor Electrodes with High-Energy and Power Densities Prepared from Monolithic

NiO/Ni Nanocomposites. *Angew. Chem., Int. Ed.* **2011**, *50*, 6847−6850.